Divalent benzimidazolium-based axles for self-reporting *pseudo*rotaxanes

S. Maryamdokht Taimoory*‡[a,b], Xiao Yu‡[a], Ngong Kodiah Beyeh,[c] John F. Trant*[a]

[a] *Department of Chemistry and Biochemistry, University of Windsor, 401 Sunset Ave., ON N9B 3P4 Windsor, Canada;*

[b]. *Department of Chemistry, University of Michigan, 930 N. University Ave., 2006B, Ann Arbor, MI 48109.*

[c] *Department of Chemistry, Oakland University, 146 Library Drive, Rochester, MI 48309-4479, USA*

‡ *These authors contributed equally to this work and are listed in this order for alphabetical reasons alone, the names can be provided in any order for any professional purpose.*

Emails of corresponding authors: *taimoory@uwindsor.ca*; *j.trant@uwindsor.ca*

Abstract

Mono and (bis)benzimidazoliums were evaluated both experimentally and computationally for their potential as pseudopolyrotaxane axle building blocks. Their aggregation and photophysical behavior, along with their potential to form a [2]pseudorotaxane with dibenzyl-24-crown-8, was studied through the synergistic application of 1D/2D and diffusion ordered NMR spectroscopy, mass spectrometry, ultraviolet-visible & fluorescence spectroscopy, and time-dependent density functional theory. Their photophysical behaviour was measured and modeled as a function of protonation state, solvent, and concentration. The axles show strong solvochromaticism and a very pronounced concentration-dependent optical profile, including self-quenching when a pseudorotaxane is formed. This axle with multiple recognition sites, has the potential to form pseudorotaxanes with tunable optical behavior.

Introduction

- Examples of benzimidazoles as dyes and drugs

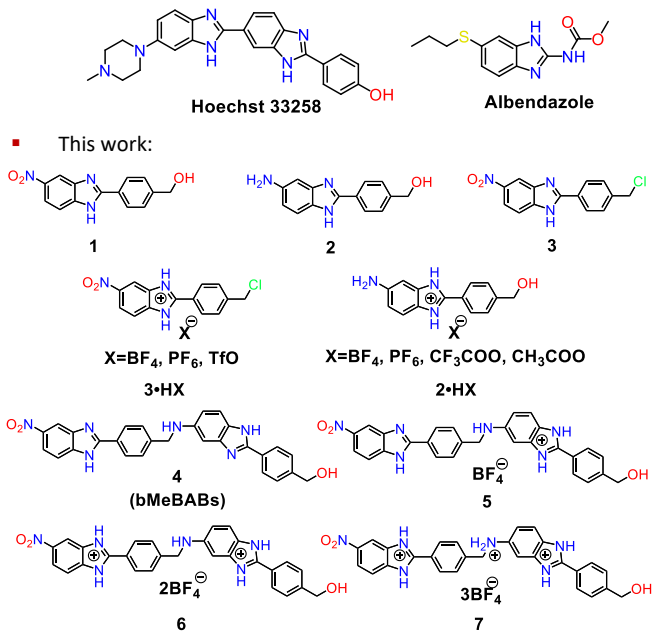

Figure 1. Some examples for previously reported benzimidazole derivatives and the novel bMeBABs and their precursors explored in this work.

The tunability of heterocyclic chromophores continuously advances as new molecular scaffolds are added to the synthetic toolbox, which in turn drives the development of materials and devices with either improved performance or unprecedented function.[1] Benzimidazole is a privileged motif, especially for incorporation into optical chemical sensors for both solid,[2] and solution state applications,[3] exemplified by biocompatible *bis*-benzimidazole fluorescent probe Hoechst 33258 and fluorescent drug Albendazole (**Figure 1**).[4]

Benzimidazoles' properties, such as their electron-accepting and π-bridging capacity, pH sensitivity/switching,[5] and ion chelating ability,[6] has made them attractive targets for a wide range of applications including optoelectronics,[7] photovoltaics,[8] solvatochromic probes,[9] photocatalysts,[10] corrosion inhibitors,[11] and molecular recognition.[12]

It is in this last application that the multifunctional nature of the benzimidazoles truly

comes into its own as their basicity and structural rigidity makes them potential guests for crown ether macrocycles.[13] *Bis*-benzimidazoliums with two fluorophores in close proximity, but not in conjugation, offer significant opportunities for the design of new materials.[14] To our knowledge the aggregation, photochemical, and chemical behavior of bis-, tris-, and oligomeric-benzimidazole units with pseudo-degenerate[15] recognition sites has not been explored.

As a part of our interest in tunable supramolecular recognition systems, we have been aiming to prepare *pseudo*rotaxanes[16] incorporating bis(methylene-bridged-2-arylbenzimidazoles) (bMeBABs) to exploit their exceptional binding affinity for crown ether macrocycles (**Figure 1**);[13a, 17], [18] protonated benzimidazoles themselves are only moderately effective as crown ether templates with limited affinity,[19] but substituted systems have well established affinities orders of magnitude higher with K_a values on the order of 10^5 M^{-1}.[17] However, we noted that our simple monomeric model systems, where the benzimidazoliums are connected through a methylene spacer, showed curious photophysical behavior (**Figure 1**). This work summarizes our exploration of these seemingly simple bMeBABs, including their photophysical, aggregative, and polymerization behavior and a preliminary investigation of their potential as axles for [2]*pseudo*rotaxanes.[13a-c, 14, 20] These are challenging systems to characterize as their solution-phase properties change as a function of ionization, concentration, and solvent. The experiments were paralleled by time-dependent DFT (TD-DFT) calculations that support the experimental results and demonstrate that the complex molecular orbitals on these systems lead to the observed properties and possible use as colour changing sensors for noting the formation of complexes such as pseudorotaxanes.[21]

Results and Discussion

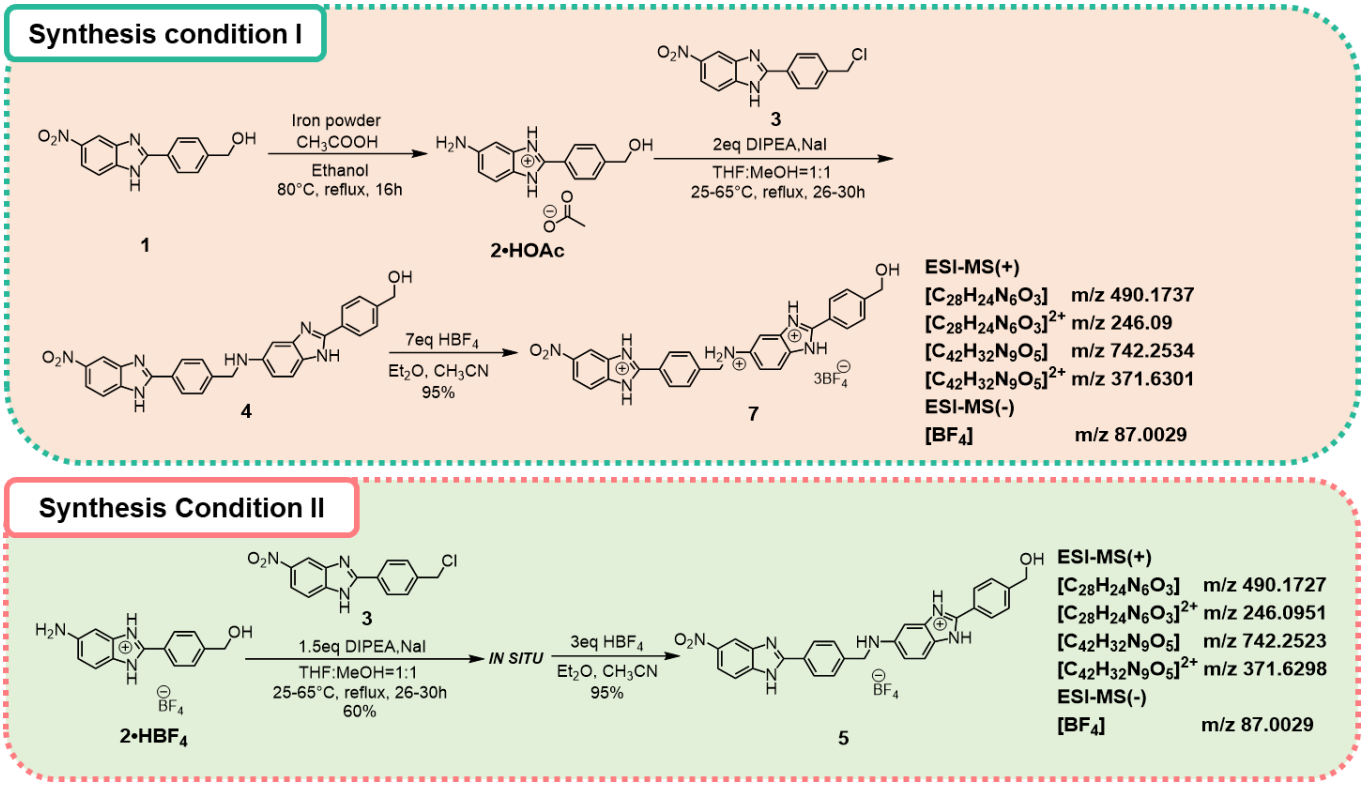

Scheme 1. Synthetic strategies used to access tri-protonated **7**, and mono-protonated **5**, and neutral **4** from precedented **1**.

Photophysical behaviour varies greatly as a function of protonation state and charge density.

Benzimidazole precursor **1** was synthesized according to published procedures (See Supporting Information).[22] To access the bis-, tris-, oligomeric, and polymeric homologs, **1** was reduced to **2·HOAc** (**Scheme 1**) and coupled with chloride **3** to provide bMeBAB **4** which features readily ionizable chromophores consisting of two phenyl-benzimidazoles separated by a methylene group.

We hypothesized that by tuning the amount of HBF_4 added, we could control the degree of protonation of the system (**Scheme 1**). Consequently, neutral **4** was treated with HBF_4 in acetonitrile at 25 ºC using two different conditions and conversion to the benzimidazolium salts was monitored by ^{1}H-NMR spectroscopy, confirmed using positive and negative mode ESI-MS and UV-Vis spectroscopy, and correlated with DFT calculations. The assigned fully tri-protonated **7** is accessed through addition of excess

HBF_4 (7 equiv.) to **4** in acetonitrile followed by precipitation with diethyl ether until no more precipitate crashed out of the solution. Using smaller amounts of HBF_4 generated a mixture of **5**, **6** and **7** which were challenging to characterize. Consequently, a different approach was required to provide better control. Under condition II, an already protonated monomer, **2·HBF$_4$,** was coupled with **3** in the presence of 1.5 equivalents of Hünig's base. *In situ* addition of three equivalents of HBF_4, followed by precipitation provides mono-protonated **5**. Adding additional HBF_4 can drive protonation through to **7**. The di-protonated species (**6**) could not be cleanly isolated without contamination from either the mono or tri-protonated species and remains a prophetic compound. Dimers **4**, **5** and **7** exhibited distinct photophysical behaviour (**Figure 2**). The differences in the ^{1}H NMR spectra of these compounds are consistent with the expected changes in electron density (**Figure 3**, **Table S1**).

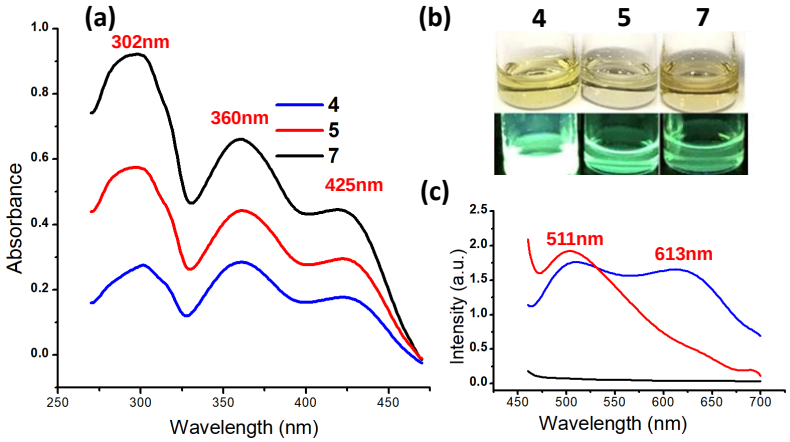

Figure 2. (a) The UV-Vis spectra of **4**, **5** and **7** (0.03 mM) in DMSO-d_6 dried with molecular sieves dried (b) pictures of **4**, **5** and **7** (0.03 mM) in dry DMSO-d_6 under both ambient and λ=365 nm light; (c) The fluorescence spectra of **4**, **5** and **7** (0.03 mM) in dry DMSO-d_6 when excited at 450 nm.

Although we are not able to conclusively assign the state of protonation by mass spectrometry, the ESI-MS spectra of both **5**, and **7**, support the proposed structures, with molecular ions consistent with both mono and di-protonated species (m/z 491 & 246

respectively). Spectra obtained in negative mode are consistent with BF_4^- present in both **5** and **7** (and not in **4**), supporting the identity of the counterion. These spectra are reproducible from separate synthetic batches. One of the possibilities we considered is that although the solid state might be the trication, dilution of these systems in DMSO may change the protonation state; however, addition of excess acid does not materially change the NMR of dissolved **7** while it does convert dissolved **4** to match **7**, suggesting that **7** does rest as the trication (**Figure S3**).

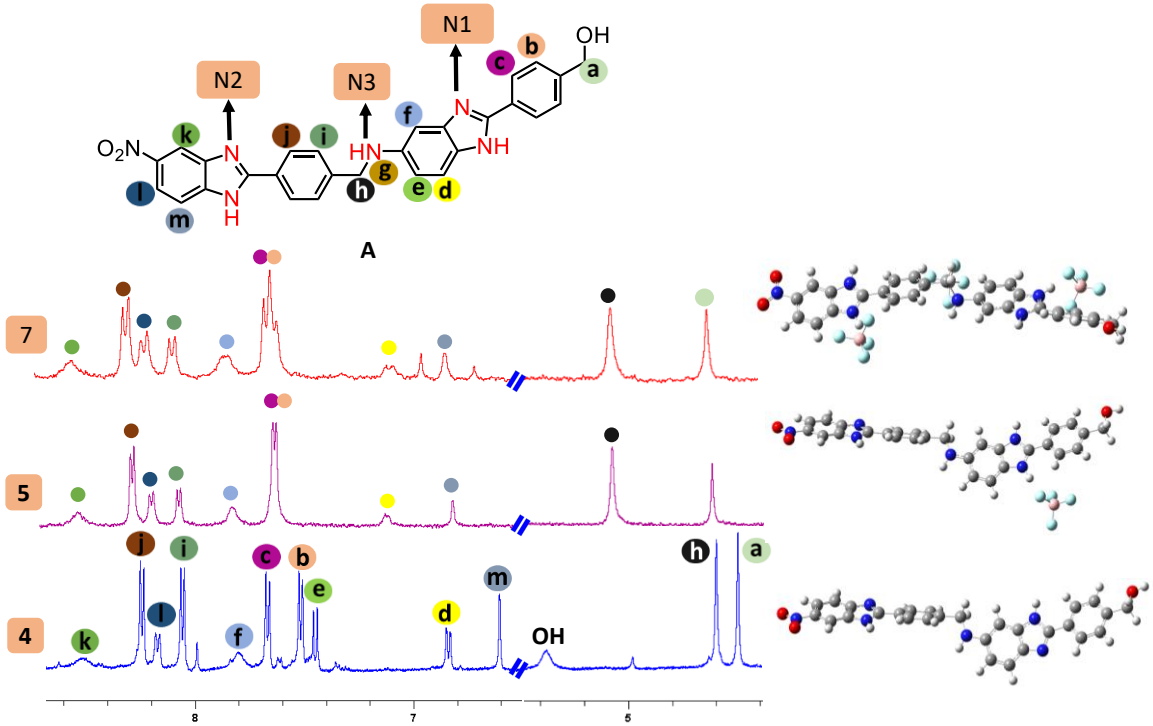

Figure 3. Partial ^{1}H NMR of neutral **4**, monoprotonated **5** and fully protonated **7**.

To obtain a more detailed understanding of these materials and the protonation process, DFT calculations at ωB97XD/6-311G(d,p) level of theory were conducted. The minimum energy structures of **4**, **5**, **6** and **7**, were determined (**Figure 4, Figure S1**).

Comparing the energetics of each possible mono-, di-, and tri-protonated skeleton in both gas phase and DMSO (IEFPCM solvation model), and either in the presence or absence of counterions, strongly suggested that the most probable species at each protonation stage was consistent with intuition (**Figure 4**; see **Figure S1** for the other,

higher energy, protonated mono- and bis- skeletons). The electron-rich benzimidazole's

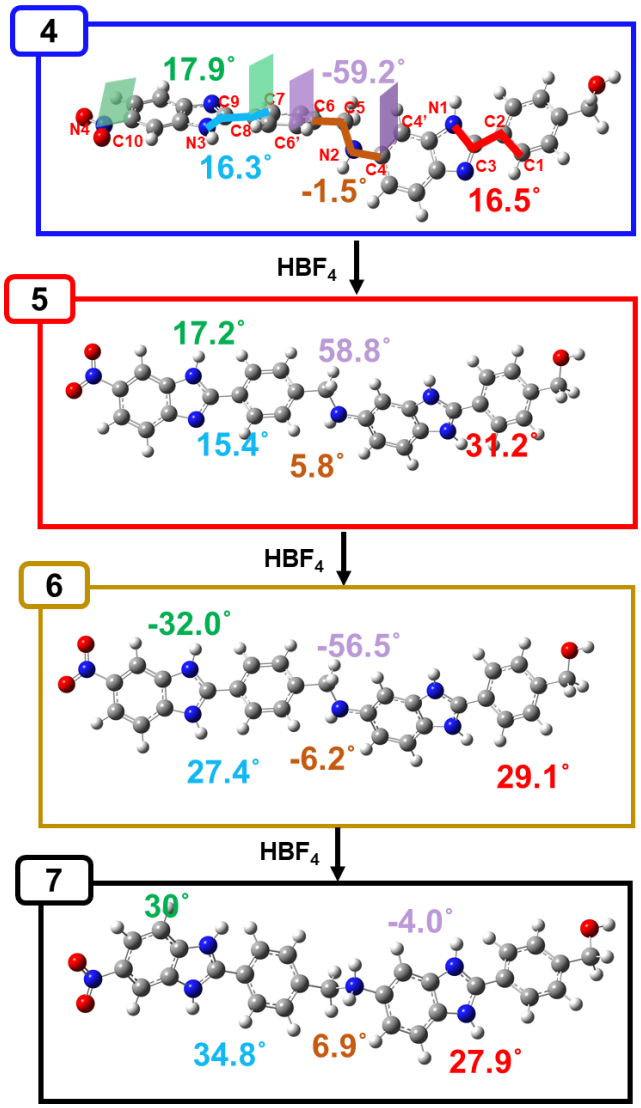

Figure 4. The ωB97XD/6-311G(d,p) calculated minimum energy structures of neutral and protonated dimeric skeletons.

N1(assigned in **Figure 3**) is the most basic site, followed by N3 on the nitro substituted benzimidazole, with the aniline N2 being the third most basic site. Protonation, however, significantly distorts the conformation of these systems (**Figure 4**). The benzimidazolium and phenyl rings are 16.5° (red) and 16.3° (blue) from coplanar in **4**, maintaining conjugation. However, protonation bends the electron-rich system out of alignment to 31.2° (red) in **5** (no significant change to blue as this ring is not protonated), and a predicted 29.1° (red) and 27.4° (blue) in the bis-protonated **6**, and fully protonated

7 (27.9° red, and 34.8° blue), respectively; breaking conjugation. This would be expected to impact donor-acceptor charge transfer, likely affecting the resulting properties. We see similar deviations from the ideal for the electron poor benzimidazole, and even in the geometry of the nitro group with the benzimidazole. Surprisingly, we do not predict any dissociation of the counterions from the bMeBAB in DMSO even for **7**, despite this generally arising in our studies of other ion-paired systems.[23]

These distortions are expected to affect the photophysical behaviour of these molecules due to their impact on the key molecular orbital (MO) energies. Both the calculated MOs and the other parameters extracted from TD-DFT were estimated using B3LYP/6-311+G(2d,p), in DMSO. The frontier orbitals, LUMO+2, LUMO+1, LUMO, HOMO, and HOMO-1, HOMO-2 were calculated and visualized (**Figure 5**, **Figure S2** and **Table S2**).

The likeliest electronic transitions, those observed by spectrophotometric methods, are not purely dependent on the energy gap between the orbitals but are also affected by the oscillator strength (f) and the other factors affecting the quantum yield. Thus, the most likely transitions, and consequently the key MOs involved, were identified by balancing maximizing f and minimizing excitation energies ($E_{excitation}$). These calculations predict $\lambda_{abs,\,max}$ (**Figure S2** and **Table S2**).

The energy gap between the HOMO (-5.38 eV) and LUMO (-2.87 eV) of the benzimidazole moiety of **4** is lower than those of **5** (HOMO -7.84, and LUMO; -0.73 eV) and **6** (HOMO -7.94, and LUMO; -1.37 eV). Fully protonated **7** behaves differently. Its energy gap (HOMO, -9.23 eV; LUMO, -1.48 eV) is far higher than those of the other protonated states.

According to our experimental absorption, (**Figure 2**), the absorption spectra of the neutral (**4**), mono- (**5**), and tri-protonated (**7**) have similar shapes, while the absorption

coefficients increase in the series **4**, **5**, and **7**. Consistent with this observations, the predicted energy of the lowest electronic transition accessible through absorption, (lowest optical transition, the optical gap) obtained from the TD-DFT calculation,[24] shows similar photophysical behaviour for **4**, **5**, and **6** but different absorption for fully

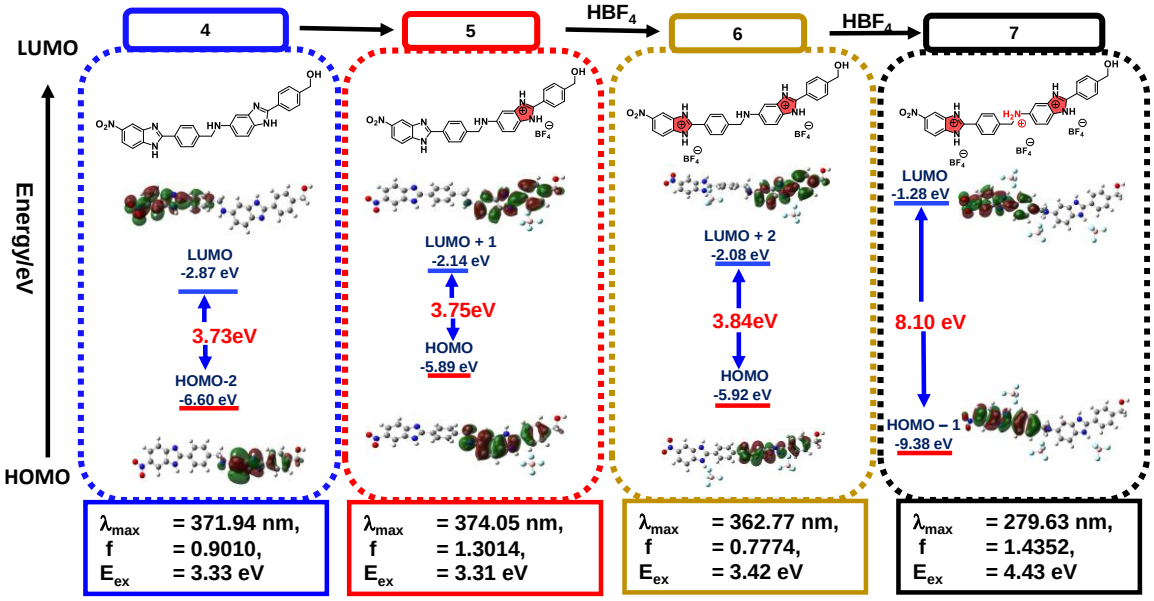

Figure 5. The DFT predicted molecular orbitals, band gap, and the TD-DFT calculated optical parameters of neutral and different protonated skeletons.

protonated state **7** (**Figure 5**). For **7**, a relatively short $\lambda_{abs,\,max}$ is predicted (4.48 eV = 277 nm) compared to **4** (4.11 eV = 301 nm), **5** (4.03 eV = 308 nm), or **6** (4.05 eV = 306 nm).

The rationale for why the value of $\lambda_{abs,\,max}$ for **7** deviates significantly from this ideal (whereas **4** and **5** behave as predicted, **Figure 2**) is not clear, but it can be due to factors including the formation of aggregated forms in solution, consistent with the excitation wavelength dependent emission event. As we discuss below, aggregation certainly occurs.

Protonation is known to decrease conjugation in aryl-benzimidazole systems, altering electron accepting ability and inducing changes in colour and photophysical behaviour.[25] The differential behaviour of **4, 5** and **7** was the phenomenon that initially

elicited our interest in this current study, solutions of the former fluoresce under ambient light while those of the latter two are more muted. To quantify this result, we measured their protonation-dependent photophysical response at 0.03 mM in dried DMSO-d6 pre-dried over molecular sieves[26] (**Figure 2**). Each molecule responds differently. All demonstrate long-wavelength bands at around 302 nm (the principal peak in the UV-Vis spectrum) albeit with different intensities. The two lower-energy absorption bands around 360 and 425 nm are lower intensity, except in **4** where all three are similar. We propose that the 302 nm peak likely arises from the free molecules as it is consistent with the calculated $\lambda_{abs,\ max}$, while the two peaks at longer wavelengths (360 nm and 425 nm) likely represent the interference from hydrogen-bonded dimer aggregation, or are due to other π-π*, n-π* transitions that are easier to access in the aggregates. A complete emission spectrum was obtained by excitation at two different wavelengths, 300 and 450 nm. Others have reported the emergence of similar new red-shifted absorption bands as a function of aggregation for both benzimidazole skeletons and other dyes.[27]

As shown in **Figure 2a**, upon protonation of neutral dimer **4**, the absorption intensity increases significantly, accompanied by a moderate change in the $\lambda_{abs,\ max}$. The absorption and emission spectra of neutral skeleton **4** are like those of monoprotonated **5**; however, **5** exhibits a stronger UV-Vis intensity than **4**, and they differ on their fluorescence $\lambda_{ems,\ max}$ (**Figure 2c**). When excited at 365 nm the longer wavelength, fluorescence of fully protonated **7** is effectively quenched, precisely consistent with computation (**Figure 2c**), and as would not be expected for any of the other protonation states, further supporting the characterization and supporting the solution-phase existence of this tri-cation. The dual fluorescence behaviour in these skeletons can be ascribed to a combination of local excitation of the electrons from the benzimidazole π to the benzimidazole π*, and variations in the intramolecular charge transfer (ICT) due

to changes in the relative conformation, geometry, and distance between the benzimidazoles. The conjugated nature of bMeBABs makes ICT the likely dominant mode of transition; this would be highly sensitive to conformational effects that break conjugation. We propose that the presence of photo-induced electron transfer between the benzimidazolium units coupled with a reduced degree of π-conjugation between the phenyl and benzimidazolium moieties as they contort out of planarity upon protonation, is responsible for the observed photophysical behavior. This is exacerbated by the change in the angle of the nitro group on the electron-poor system as it also distorts out of conjugation as protonation increases (**Figure 4**). This effect arises from both changes in electron density and steric pressure from the counterions trying to mask the charge.

This decrease in conjugation across all moieties of the molecule in **7** will affect the excitation and charge transfer processes and should lead to fluorescence quenching. In contrast, for both neutral **4** and monoprotonated **5** (and putative **6**)**,** electrons can transfer from the donor phenyl-benzimidazole to the acceptor system (**Figure S2, Table S2**). The differential behaviour as a function of protonation shows this system's sensitivity to its environment. This photophysical behaviour is of more than academic interest, as if it is further affected by the formation of *pseudo*rotaxanes, it can be used as a simple chromatic sensor for supramolecular complex formation; a far simpler read-out than relying on complex intersectional multi-instrumental analytical techniques. This *in situ* characterization would make these even more privileged structures. To explore this possibility, we first investigated the aggregation and solvent-dependent behaviour.

Photophysical response varies as a function of solvent and concentration/aggregation.

As we seek to use these for self-assembly applications, and as aggregation appears to be

a challenge at even low concentrations regardless of protonation state, we needed to better understand the relationship between aggregation state, solvent choice, and analyte concentration in these systems. As the tri-protonated species would best be able to chelate to cation-recognizing macrocyclic units, and hence the most useful for any application; this species, **7**, which alone of the examined species was effectively non-fluorescent at 0.03 mM in DMSO when irradiated at 450 nm, was used for all further studies.

The UV-Vis absorption spectra (300-450 nm) of fully protonated axle **7** were collected over a large concentration range in several solvent systems. The low energy $\lambda_{abs,\ max}$ peak of **7** exhibits an extreme concentration-dependent red-shift (**Figure 6a**) to higher wavenumbers as the concentration increases. This peak is not present in samples with concentrations of 0.1 mM or below. We admit that at these concentrations we are saturating the detector, but as these are potentially relevant concentrations for our studies in the future, this cannot be avoided. Although this means that the amplitude of the signals is meaningless and should not be considered, the wavelengths of the maxima still vary in a regular fashion which is curious. Changing photophysical behaviour is also apparent from the colour of the solution: decreasing the concentration of axle from 3 mM to 0.01 mM in DMSO, leads to a significant change in the color from a deep yellow to colourless (**Figure 6c**). The colour gets fainter and fainter and then disappears at 0.1 mM, the same "cut-off" value as noted in the UV-vis data for the disappearance of this peak in the yellow. The bMeBAB also exhibits significant linear fluorescence enhancement upon increasing of the concentration; overcoming the fluorescence quenching observed at 0.03 mM concentration (see above, **Figure 6b**) with a distinct blue-green emission centred at 528 nm (**Figure 6b**). A concentration-dependent

decrease is clearly observed down to 0.3 mM, but it drops off markedly below this point.

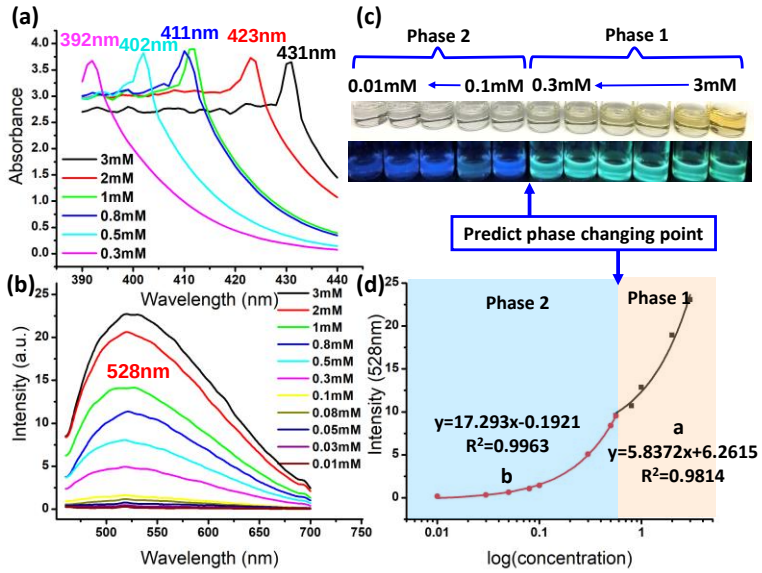

Figure 6. (a) The UV-Vis spectra of 3 mM-0.3 mM **7** in undried DMSO; (b) the fluorescence spectra of **7** in undried DMSO (3 mM-0.01 mM) with excitation at 450 nm; (c) photographs of the samples of **7** used to generate Figure 5 under ambient light (top) and under excitation at 365 nm (bottom) in undried DMSO; (d) fluorescence intensity plotted against concentration with the equations of the two curves. (Note the discontinuity at 0.3 mM).

This discontinuity in behaviour is clearer when the data is plotted (**Figure 6d**), showing that we have two different mechanisms of fluorescence in play. We believe that this may be attributed to aggregation induced emission behaviour.

Absorption/emission shifts like that in **Figure 6a** are known but are very rare and we are unaware of any system with such a drastic change over such a small concentration change.[28] The shift likely arises from a combination of the emergence of a new species that replaces the computationally calculated energy minimum (**Figure S1, S2**); the emergence of additional non-covalent, ion-pairing and Hydrogen bonding (H-bonding) interactions between functional groups on adjacent axles; the restriction of molecular rotation and vibration due to aggregation; and/or the interference of intramolecular charge transfer by intermolecular processes due to the increase in concentration. To try to narrow down the contributing causes we attempted to disrupt the aggregates by changing the solvent, believing that the trace water in the DMSO could be affecting

solvation, as reported for similar systems.[29]

Employing DMSO-d_6, pre-dried over previously washed 4 Å molecular sieves, induced no change in the fluorescent behaviour, but did induce a red-shift compared to the slightly wet sample (**Figure S4; Table S3**). Considering that water could be expected to break-up aggregates, and that aggregates are likely responsible for the extreme shift in the $\lambda_{abs,\ max}$, one would anticipate that a solution in wet DMSO would behave like a lower concentration sample in DMSO in terms of aggregation (**Figure S4; Table S3**).

We investigated the concentration-dependent photophysical behaviour of **7** in both wet DMSO and DMF (10% v/v H_2O in each). By inspection, adding water makes a big difference (**Figure 6** vs **Figure 7** and **Figure S5**), likely affecting aggregation and/or

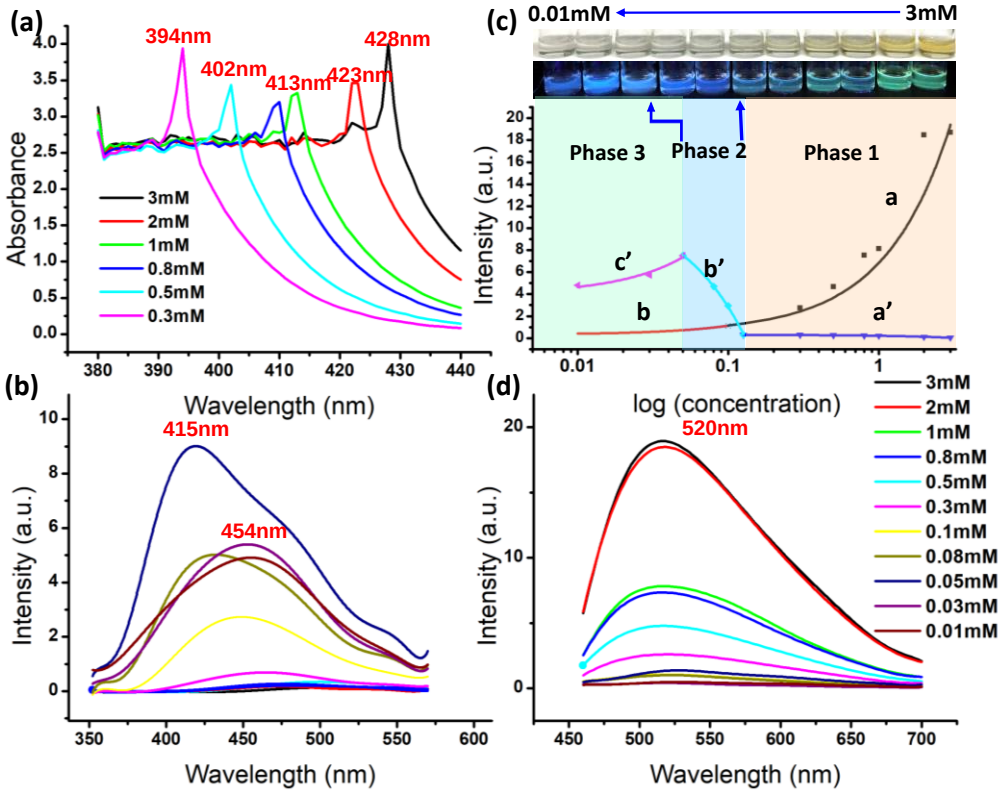

Figure 7. (a)The UV-Vis spectra of **7** (3 mM-0.3 mM) in 9:1–DMSO:H_2O; (b) The fluorescence spectra, excited at 300 nm of **7** (3 mM-0.01 mM) in 9:1–DMSO:H_2O; (c) ambient light (top), excitation at λ=365 nm (bottom) appearance of **7** in 9:1–DMSO:H_2O; (d) The fluorescence intensity of various concentrations at 520 nm emission (black, red) and 415nm emission (blue, cyan, pink); (e) The fluorescence spectra, excited at 450 nm, of **7** (3 mM-0.01 mM) in 9:1–DMSO:H_2O

conformational distribution and consequently, its photophysical properties. Water likely better solvates these polycations, disrupting aggregation.

The presence of 10% H_2O within the solution, keeps the solutions colorless at higher concentrations than does pure DMSO (**Figure 7c**, **Figure S5c** vs **Figure 6c**); this suggests that the yellow tint may arise from aggregates rather than from the monomer alone. Increasing the concentration of **7** in the 10% H_2O in DMSO solution from 0.3 mM to 3 mM leads to a U-shaped curve in amplitude and the same definite red shift in the $\lambda_{abs,\ max}$ as was seen in dry DMSO; curiously, the peaks are sharper in this spectrum than they were for pure DMSO. Again, like before, this peak is not present at concentrations 0.1 mM or below. The fluorescent behaviour is more complicated in this mixed solvent system. As the concentration of **7** rises from 0.01 to 0.05 mM, the fluorescence emission at 400-450 nm (excitation at 365 nm) gradually increases (**Figure 7b**), with a significant shift in the $\lambda_{ems,\ max}$. As the concentration continues to rise, the amplitude starts to fall to 0, and fluorescence is effectively fully quenched at concentrations above 0.5 mM. Conversely, when excited at 450 nm, we see a steady increase in $\lambda_{ems,\ max}$ at 520 nm, effectively reaching maximum signal at 3 mM (**Figure 7d**). This differential behaviour suggests that an isolated molecule, or more likely a dimer, emits at 415 nm, but that this band is quenched as aggregates start to form as the concentration increases. The concentration of monomer above the critical aggregation concentration (CAC) would remain constant and we would not expect to see a decrease in emission, but rather a stabilization. It is likelier that the 415 nm peak is due to a lower ordered aggregated form or a different aggregate that effectively ceases to exist as the concentration continues to rise, producing species that emit at 520 nm.

Therefore, **7** experiences a concentration dependent, two-phase (Phase 1 is between 3 mM to 0.3 mM and phase 2 is 0.1 mM to 0.01 mM), aggregation process with each aggregate form having its own relationship between concentration and emission maximum (**Figure 7c and 7d**). Changes in absorption at the lower concentrations (0.01

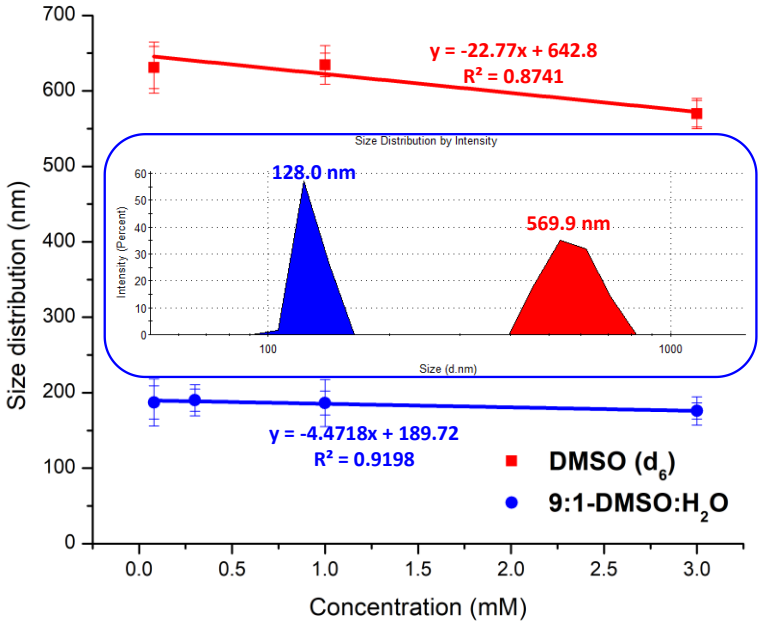

Figure 8. Linear trend between concentration of **7** and solvodynamic radius in the different solvent systems. In neither system were particles observed below 0.1 mM. Data must be interpreted carefully as DLS can be unreliable for fluorescent samples.

to 0.5 mM) are extremely sensitive to small changes demonstrating the potential of fully protonated **7** to act as a chemical sensor. Interpolation suggests the mechanism changes at 0.56 mM, however there is clearly a transition zone between 0.5 and 0.3 mM where we have a mixture of the mechanisms coexisting.[30]

We considered that the effect could arise due to changes in solvent viscosity, so to discount this possibility we examined **7** in a 9:1–DMF: H_2O system (**Figure S5**). Consistent with the DMSO system, increasing the concentration of **7** enhanced the intensity and appearance of sharp absorptions in the UV-vis spectrum as in **Figure 6a** and **7a**. This is not solvent specific behaviour; it appears to be a feature of the molecule.

To provide supportive evidence of this aggregation behaviour, we employed dynamic

light scattering (DLS, **Figure 8**). The DLS data shows that aggregates are present, and that the size varies based on solvent, but is little affected by concentration above 0.08mM; below 0.08mM particles are not observed by DLS. The monomers would not be expected to be detectable. This threshold value might consequently be close to the CAC. This is very close to the 0.1M cut-off we observed in the data, strongly supporting our contention that the unusual photophysical behaviour arises from aggregation. The lines in the DLS are essentially flat within the error of the measurements, indicating that a single species seems to dominate the aggregation form regardless of the concentration once the CAC is attained (**Figure 8**). Consistent with the above observations, using mixed solvent systems changes the particles that are present: they are far smaller (100 nm vs 600 nm at 3 mM concentration) when water is introduced, again supporting our hypothesis that water disrupts the aggregates by better solubilizing the tri-cations and their conjugate anions. But again, an aggregate is observed across this concentration range, with nothing detectable by DLS below 0.08 mM suggesting that this might be close to the CAC for this compound in both solvents, again inline with the photophysical response. This concentration of bMeBAB is far lower than will be employed for the supramolecular assembly chemistry we intend to use these systems for, suggesting that aggregation might be a serious concern. Polymers, rather than these simple model dimers, will be used at a lower molarity (although a higher mass concentration) and are likely to behave differently and will need to be investigated separately. Regardless, these results suggest that our planned chemical functionalization of the aryl rings to increase solubility and tune macrocycle affinity, will likely be necessary, as these unsubstituted bMeBABs are insufficiently soluble and prone to aggregation.

Both the photophysical and sizing data strongly suggests that a single class of

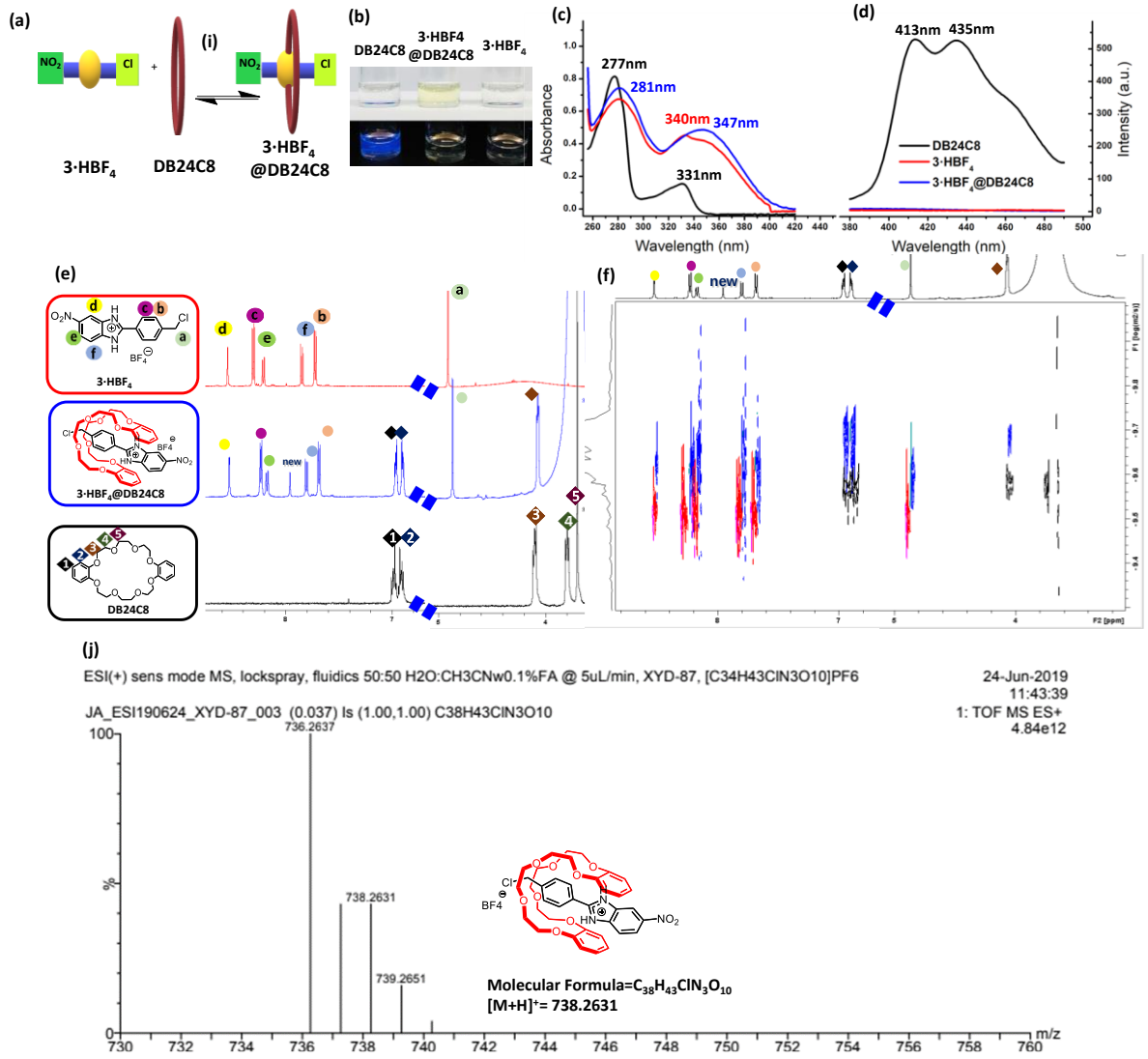

Figure 9. *Pseudo*rotaxane formation. (a) synthesis route toward **3·HBF$_4$@DB24C8**, (i) $CHCl_3$, 25 °C; (b) ambient light, excitation at λ=365 nm appearance of host, guest and [2]*pseudo*rotaxane in pure dry DMSO-d_6; (c, d) UV-vis-Fluorescence spectra of host, guest and [2] *pseudo*rotaxane in DMSO;. The measurement of UV-Vis-fluorescence was carried out with 0.3mM solution of isolated host, guest and [2] *pseudo*rotaxane (**3·HBF$_4$@DB24C8)** in DMSO-d_6. (e) From top to bottom are ^{1}H NMR in DMSO-d_6 of 3 mM solution of **3·HBF$_4$** (guest), 3 mM solution of **3·HBF$_4$@DB24C8** and 3mM solution of **DB24C8** (host). (f) 2D DOSY NMR spectra (300 MHz, DMSO-d_6) of **3·HBF$_4$@DB24C8**. (g) ESI-MS(+)spectra of **3·HBF$_4$@DB24C8.**

aggregate is formed at higher concentrations, and that this aggregate begins to emerge above 0.08 mM. Addition of water weakens the interactions resulting in smaller aggregates, but it does not change the CAC. These aggregates show remarkable concentration-dependent red- shifting making them extremely curious structures deserving of further study.

Poly(bMeBABs) are promising axles for the generation of poly(pseudorotaxanes). *Pseudorotaxanes* should be readily formable with complementary macrocycles such as crown ethers. We begin this investigation using a combination of ^{1}H NMR, high resolution mass spectrometry (HRMS), liquid chromatography–mass spectrometry (LC-MS), UV-Vis and fluorescence spectroscopy as the fluorescent behavior of the bMeBABs makes them their own sensors. We began our investigations with the most soluble monomeric precursor of **3,** its HPF_6 salt, **3•HPF$_6$** (**Scheme S2**, **Figure S6 and S7, and Table S4**), but switched to using **3•HBF$_4$** as we found the chemistry more reproducible. After screening several crown ethers (**Figure S8-S10**), dibenzo-24-crown-8 (**DB24C8**) was both computationally predicted, and experimentally demonstrated, to be a good match size-wise (21 atoms was insufficient, preventing threading, while 27 was excessive and assembly was difficult to detect). The optimized geometries of the various potential host-guest complexes obtained from tuning either the counterion (**Figure S11**) or the host (**Figure S12**) indicate that both **2•HBF$_4$@24C8** and **3•HBF$_4$@DB24C8** provide the most favorable host-guest interaction energy and optimal solvation free energy. The latter's inherent fluorescence makes it more useful for the current study.

We obtained the [2]*pseudo*rotaxane, **3•HBF$_4$@DB24C8**, by combining the two components in CH_3Cl at room temperature. The complex was then treated with **2•HBF$_4$** to attempt to make the [2]*pseudo*rotaxane of bMeBAB **7** (**Figure 9, Figure S13**). However, after purification, only uncoordinated dimer **7** and a small amount of residual **3•HBF$_4$@DB24C8** were isolated. The latter is distinguishable from the uncoordinated **3** due to moderate changes in the ^{1}H NMR chemical shifts of the aryl protons as a result of NH···O hydrogen bonding, CH···O and π-stacking interactions between the electron poor benzimidazolium and phenyl rings of the axles and the electron rich rings of

DB24C8 (**Figure 9e; Table S5**). This is suggestive of complexation, but the data could equally arise from an *exo* complex, a face-to-face interaction occurring outside of the cavity as from a more traditional *endo* complex, where the **3** inserts into the crown ether. The former is likelier to be more transient than the latter but can't be ruled out based on the small shifts from the ^{1}H NMR.

Similarly, **3•HBF$_4$** has two absorbance maxima in the UV-Vis spectrum at 281 nm and 340 nm, while **DB24C8** absorbs at 277 nm and 331 nm (**Figure 9b**). When the two are mixed together, the axle dominates the spectrum, but there is no evidence of the **DB24C8** peak at 331 nm; instead, there is a slight red-shift to 347 nm with a concomitant increase in signal amplitude. This is also seen at the lower wave-number signal where the intense **DB24C8** absorbance at 277 nm completely disappears, and the mixture exhibits a stronger signal at 281 nm resembling the free axle. **DB24C8** is highly fluorescent (**Figure 9d**), with emission at 413 nm and 435 nm (when excited at 370 nm); however, these two emission peaks are completely quenched in the mixture. Finally, this effect can be seen with the naked eye (**Figure 9c**). In ambient light, both isolated **DB24C8** and **3•HBF$_4$** are colorless; however, the 1:1 mixture is yellow (0.3 mM, DMSO-d$_6$, room temperature). When excited at λ=365 nm, **DB24C8** is highly fluorescent, but neither **3•HBF$_4$** nor the mixture of the two molecules are; the interaction is good enough that the axle quenches the crown ether's fluorescence. **DB24C8** does not exist as an optically-active independent species when in a 1:1 ratio with **3•HBF$_4$** in DMSO. However, the diffusion ordered NMR spectroscopy (DOSY NMR), photophysical, and mass spectrometric analyses all suggest that **3•HBF$_4$@DB24C8** is a strongly associated *endo* complex (**Figure 9**, **Figure S13**). 2D DOSY visualizes diffusion; **DB24C8** and **3•HBF$_4$** have different solvodynamic radii and different rates of diffusion.[31] However, if they assemble, they would show the same rate of diffusion,

and this is what is observed (**Figure 9f and S13C**).

DOSY and mass spectrometry supports the formation of a tight complex.

DOSY NMR is a suitable technique to probe assemblies in solution.[32] A smaller diffusion coefficient indicates a larger species when in the same solvent, same concentration, and same temperature.[33] The diffusion coefficients for the free axles **3**, and **7**, and the **DB24C8** all reveal smaller species (**Figures S34-36**). It also shows **7** to be larger than **3**. One interesting feature we observed with axle **7** is that, without sonication before DOSY measurement we see a larger species, which is attributed to self-aggregation. When sonicated 5 minutes before DOSY measurement, these aggregates are disrupted, and we see monomeric **7** approaching the size of **3**. The differences are easily attributable to the presence of the counterions, and the required solvation shell associated with the charged species. The diffusion coefficients of these components when they are mixed together are all consistent with their incorporation into the same, much larger species. Take **DBC24** as an example, on its own the average diffusion coefficient is $2.62\pm0.04\times10^{-10}$ m^2s^{-1}. This value changes to $1.93\pm0.04\times10^{-10}$

m^2s^{-1} in **3•HBF$_4$@DB24C8**, and to 1.60±0.01×10^{-10} m^2s^{-1} in **7@DB24C8**. These values

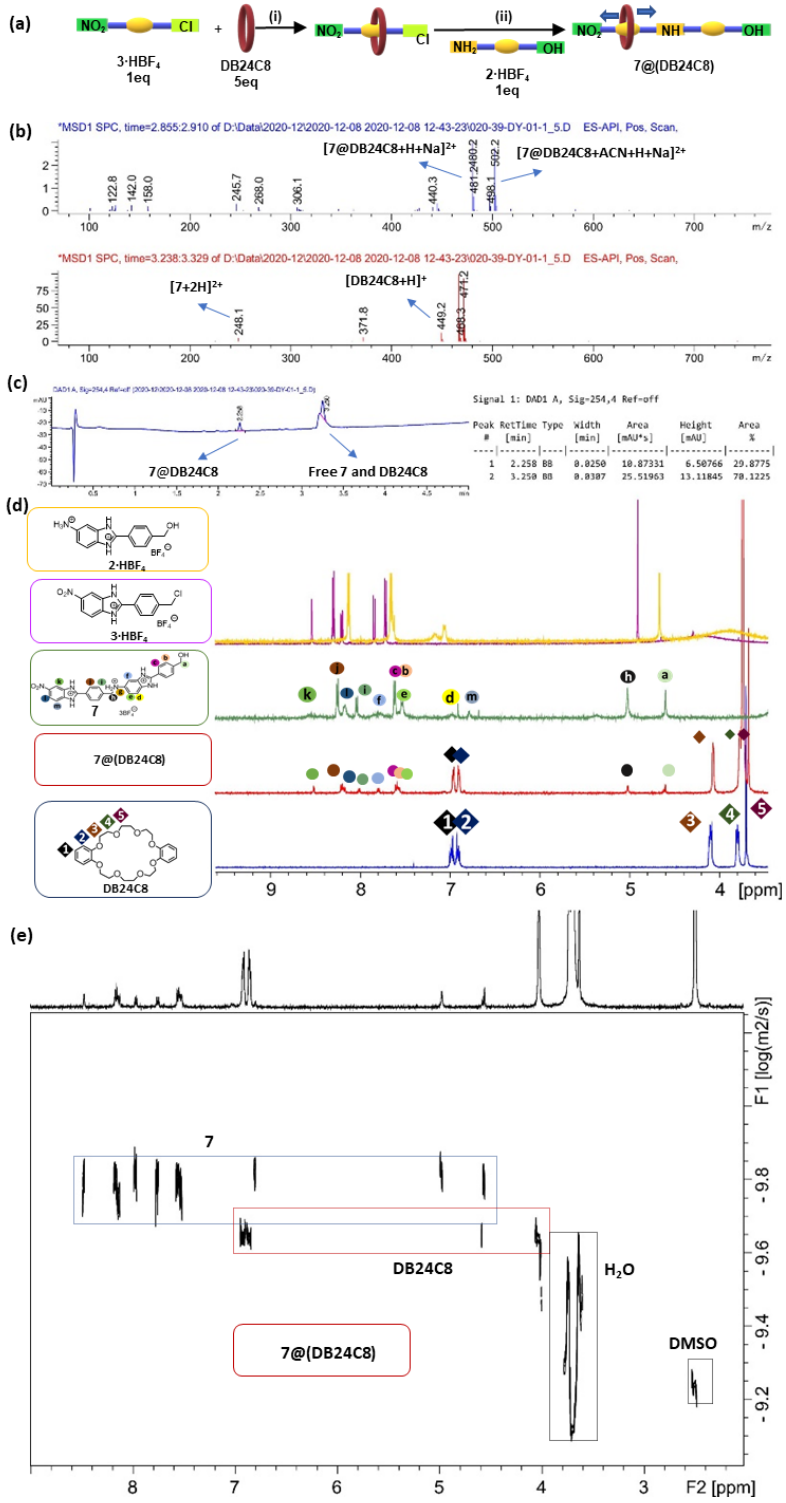

Figure 10. (a) Synthetic route toward **7@DB24C8**, (i) CH_3CN/H_2O, 25°C, (ii) 0.2 equiv. NaI, 50°C. (b) MS(+)spectra of **7@DB24C8 (top)** ,and free **7** and **DB24C8** (bottom). (c) LC spectra of **7@DB24C8**. (d) From top to bottom are ^{1}H NMR in DMSO-d_6 of 3 mM solution of **2·HBF$_4$** (orange), **3·HBF$_4$** (pink), **7** (guest, red), 3 mM solution of **7@DB24C8** (blue) and 3mM solution of **DB24C8**(host, black). (e) 2D DOSY NMR spectra (300 MHz, DMSO-d_6) of **7@DB24C8**.

confirm the **DB24C8** is part of a larger species in **3•HBF$_4$@DB24C8**, and an even larger species in **7@DB24C8**. These can also be seen from the hydrodynamic radii calculated from the Stokes-Einstein equation (**Table 1**).

^{1}H NMR titration was conducted to delineate the interaction between the axle **7** and **DB24C8**. In the experiment, **DB24C8** was titrated against **7**. To enhance threading, the NMR sample was sonicated for two minutes after each addition. The axle's (**7**) signals were monitored as a function of concentration of **DB24C8** added, and winEQNMR2 software[34] was used to derive a binding constant of K=1900±100 M^{-1} (**Figure S33**). This binding constant represents a high affinity, considering the highly competitive solvent system.

Table 1. Average diffusion coefficients D[a] ($\times 10^{-10}$ m^{2}s^{-1}) of the species and the respective hydrodynamic radii r (nm) in different combinations in 9:1–DMSO-d_6:D_2O [b] v/v at 298 K.

System	*D*	r	System	*D*	r
3.BF$_4$	2.96	0.69	**3** in **3@DB24C8**	2.34	0.87
DB24C8	2.62	0.78	**DB24C8** in **3@DB24C8**	1.93	1.06
7	1.29	1.59	**7** in **7@DB24C8**	1.53	1.34
7 with sonication	2.15	0.95	**DB24C8** in **7@DB24C8**	1.60	1.28

[a] Standard deviation < 5%. [b] Average diffusion coefficient of DMSO-d_6 in the 9:1–DMSO-d_6 :D_2O mixture is 6.97×10^{-10} m^{2}s^{-1}.

Although requiring exceptional affinity and kinetic stability of the assembly, tightly-bound *pseudo*rotaxanes sometimes survive the energies used in mass spectrometry; this

is the case here where the electrospray spectrum provides an exact match for the complex at m/z 738.2631, with an isotope pattern consistent with **3•HBF$_4$@DB24C8**. A simple *exo* (non-inclusion) complex is unlikely to survive the energies applied, strongly implying the formation of a *pseudo*rotaxane. Further evidence for the existence and kinetic stability of these bMeBAB [2]*pseudo*rotaxanes is provided through LC-MS analysis (**Figure 10, b-c**); injection of the crude reaction mixture provides two peaks with integration ratios consistent with the NMR data for the complexed and uncomplexed axle-crown ether; the peak registers m/z of 481 and m/z 502, consistent with [**7@DB24C8+H+Na**]$^{2+}$ and the acetonitrile adduct [**7@DB24C8+ACN+H+Na**]$^{2+}$ respectively. There is no evidence of either component alone. The second peak, with a clear shoulder in the spectrum, shows masses consistent with both the crown ether and the axle separately. This is extremely unusual. If the *pseudo*rotaxane was in fast equilibrium with the monomers, as we expect for these types of systems, one would not expect distinct signals. Instead, the signal would be smeared along the baseline as a single bump between the two retention times as the equilibria plays out in real time; that this is not the case strongly implies that a kinetically stable complex can be formed—clearly requiring sonication levels of energy to rearrange, as no formation is observed without sonication, and the sample appears stable for extended periods of time when maintained at room temperature or below. We were never able, over three years of effort, able to acquire a crystal suitable for X-ray analysis. This inclusion complex's ready formation does tease that higher order assemblies are viable.

These preliminary studies are highly suggestive that *pseudo*rotaxanes can be formed by our novel bMeBABs, which is very promising for the formation of higher order systems on oligomeric and polymeric derivatives. Further investigations into these polymers, their poly*pseudo*rotaxane constructs and the determination of the binding

affinity of the DB24C8 ethers for these systems are currently underway.

Conclusions

These bis(methylene-bridged-2-arylbenzimidazoles), bMeBABs, are promising colour-changing sensor scaffolds for the generation of *pseudo*rotaxanes, due to their environmentally dependent photophysical activity. The spectroscopic activity of axle alone is highly sensitive to concentration, protonation state, and solvent. As our main purpose is to develop long cross-linked molecular tubes from a *pseudo*rotaxane template, it is essential that all binding sites on the thread are occupied. Benzimidazole-crown ether interactions are a promising motif considering the measured affinity, and coupled with our knowledge that substituted systems show even higher affinity,[13c] and the sensitivity of these systems to their environment allows us to monitor protonation, assembly, and undesired aggregation. As mentioned, these systems show the greatest concentration-dependent shift in $\lambda_{abs,\,max}$ and $\lambda_{ems,\,max}$ that we are aware of in the literature for a small molecule making them particularly useful. This photophysical activity makes these possibly the simplest scaffolds for determining the presence of a supramolecular complex, an extremely fortunate accident in our chosen system. This will prove highly useful to us in our design of more complex supramolecular constructs, and we believe it will be equally useful to others.

Conflicts of interest

The authors declare no competing financial interests.

Acknowledgements

The authors gratefully acknowledge financial support for the project from the Natural

Sciences and Engineering Research Council of Canada (JFT: grant # 2018-06338), the Canadian Tricouncil (JFT: NFRFE-2018-00075), and the American Chemical Society Petroleum Research Fund New Directions Program (JFT: ACS PRF 60765-ND7). SMT and JFT wish to recognize that this work was made possible by the facilities of the Shared Hierarchical Academic Research Computing Network (SHARCNET: www.sharcnet.ca) and Compute/Calcul Canada. NKB gratefully acknowledges financial support from Oakland University, Michigan, USA.

Author Contributions.

Conceptualization, SMT, JFT; Funding acquisition JFT; Investigation, YX, SMT; Methodology, YX, SMT, NKB; Project administration, JFT; Supervision, JFT, SMT, NKB; Writing original draft, YX, SMT; Writing – review and editing, All authors.

Notes and references

[1] a) P. N. Preston, *Chem. Rev.* **1974**, *74*, 279-314; b) K. M. H. Nguyen and M. Largeron, *Chem. - Eur. J.* **2015**, *21*, 12606-12610; c) J. Kulhánek, F. Bureš, O. Pytela, T. Mikysek and J. Ludvík, *Chem. Asian J* **2011**, *6*, 1604-1612; d) P. Molina, A. Tárraga and F. Otón, *Org. Biomol. Chem.* **2012**, *10*, 1711-1724.
[2] a) Y. Cao, M. Yang, Y. Wang, H. Zhou, J. Zheng, X. Zhang, J. Wu, Y. Tian and Z. Wu, *J. Mater. Chem. C* **2014**, *2*, 3686-3694; b) V. S. Padalkar and S. Seki, *Chem. Soc. Rev.* **2016**, *45*, 169-202.
[3] a) B. Han, N. Zhou, W. Zhang, Z. Cheng, J. Zhu and X. Zhu, *J. Polym. Sci. A: Polym. Chem.* **2013**, *51*, 4459-4466; b) H. Kaur, N. Singh, N. Kaur and D. O. Jang, *Sens. Actuators, B* **2019**, *284*, 193-201.
[4] M. Ladinig, W. Leupin, M. Meuwly, M. Respondek, J. Wirz and V. Zoete, *Helv. Chem. Acta* **2005**, *88*, 53-67.
[5] E. Horak, P. Kassal and I. Murković Steinberg, *Supramol. Chem.* **2018**, *30*, 838-857.
[6] Z. Lu, Y. Liu, S. Lu, Y. Li, X. Liu, Y. Qin and L. Zheng, *RSC Adv.* **2018**, *8*, 19701-19706.
[7] J. E. Kwon and S. Y. Park, *Adv. Mater. (Weinheim, Ger.)* **2011**, *23*, 3615-3642.
[8] a) G. B. Bodedla, K. R. Justin Thomas, M.-S. Fan and K.-C. Ho, *J. Org. Chem.* **2016**, *81*, 640-653; b) G. M. Saltan, H. Dinçalp, M. Kıran, C. Zafer and S. Ç. Erbaş, *Mater. Chem. Phys.* **2015**, *163*, 387-393.
[9] E. Horak, R. Vianello, M. Hranjec, S. Krištafor, G. K. Zamola and I. M. Steinberg, *Spectrochim. Acta, Part A* **2017**, *178*, 225-233.
[10] J. Jayabharathi, V. Thanikachalam and K. Jayamoorthy, *Photochem. Photobiol. Sci.* **2013**, *12*, 1761-1773.
[11] M. Marinescu, *BMC Chem.* **2019**, *13*, 136.
[12] a) N. Perin, M. Hranjec, G. Pavlović and G. Karminski-Zamola, *Dyes Pigments* **2011**, *91*, 79-88; b) T. Chaudhuri, A. Karmakar, S. Ghosh, C. Mukhopadhyay, S. Pal and M. Banerjee, *J. Lumin.* **2015**, *161*, 164-173.
[13] a) K. Zhu, V. N. Vukotic and S. J. Loeb, *Chem. Asian J.* **2016**, *11*, 3258-3266; b) N. Farahani, K. Zhu and S. J. Loeb, *ChemPhysChem* **2016**, *17*, 1875-1880; c) N. Noujeim, K. Zhu, V. N. Vukotic and S. J. Loeb, *Org. Lett.* **2012**, *14*, 2484-2487; d) S. Ghosh, A. M. Schmiedekamp and C. Mukhopadhyay, *Tetrahedron* **2012**, *68*, 9826-9835; e) D. J. Mercer, S. J. Vella, L. Guertin, N. D. Suhan, J. Tiburcio, V. N. Vukotic, J. A. Wisner and S. J. Loeb, *Eur. J. Org. Chem.* **2011**, *2011*, 1763-1770.
[14] L. Li and G. J. Clarkson, *Org. Lett.* **2007**, *9*, 497-500.
[15] Degenerate implies perfect symmetry and equivalence; although locally the sites are very similar, sites along short oligomers are not truly equivalent.
[16] a) F. Huang and H. W. Gibson, *Prog. Polym. Sci.* **2005**, *30*, 982-1018; b) M. Xue, Y. Yang, X. Chi, X. Yan and F. Huang, *Chemical Reviews* **2015**, *115*, 7398-7501.

[17] K. Zhu, V. N. Vukotic, N. Noujeim and S. J. Loeb, *Chem. Sci.* **2012**, *3*, 3265-3271.
[18] K. Zhu, G. Baggi and S. J. Loeb, *Nat. Chem.* **2018**, *10*, 625-630.
[19] a) T. L. Price Jr. and H. W. Gibson in *Crown Ether-Based Polymeric Rotaxanes*, **2011**, pp. 151-182; b) H. R. Wessels and H. W. Gibson, *Tetrahedron* **2016**, *72*, 396-399.
[20] J. F. Stoddart, *Angew. Chem. Int. Ed.* **2017**, *56*, 11094-11125.
[21] P. Shende, B. Prabhakar and A. Patil, *Tr. Anal. Chem.* **2019**, *121*, 115687.
[22] a) H.-T. Li, S.-Y. Fan, Z.-P. Li, F.-L. Yu, X.-Q. Hu, J.-C. Cheng, P. Zhang, B.-H. Zhong and W.-G. Shi, *Chin. Chem. Lett.* **2016**, *27*, 1630-1634; b) S. J. Loeb, J. Tiburcio, S. J. Vella and J. A. Wisner, *Org. Biomol. Chem.* **2006**, *4*, 667-680; c) M. L. Richards, S. C. Lio, A. Sinha, H. Banie, R. J. Thomas, M. Major, M. Tanji and J. C. Sircar, *Eur. J. Med. Chem.* **2006**, *41*, 950-969; d) Y. Liu, Y. Lu, M. Prashad, O. Repič and T. J. Blacklock, *Adv. Synth. Catal.* **2005**, *347*, 217-219.
[23] a) S. M. Taimoory, K. Twum, M. Dashti, F. Pan, M. Lahtinen, K. Rissanen, R. Puttreddy, J. F. Trant and N. K. Beyeh, *J. Org. Chem.* **2020**, *85*, 5884-5894; b) S. M. Taimoory, V. Cataldo, A. Schäfer, J. F. Trant and R. Guterman, *Chem. - Eur. J.* **2021**, *27*, 3440-3448; c) N. K. Beyeh, I. Diez, S. M. Taimoory, D. Meister, A. L. Feig, J. F. Trant, R. H. A. Ras and K. Rissanen, *Chem. Sci.* **2018**, *9*, 1358-1367.
[24] J.-L. Bredas, *Mater. Horiz.* **2014**, *1*, 17-19.
[25] G. Sevinç, B. Küçüköz, H. Yılmaz, G. Şirikçi, H. G. Yaglioglu, M. Hayvalı and A. Elmali, *Sens. Actuators, B* **2014**, *193*, 737-744.
[26] D. B. G. Williams and M. Lawton, *J. Org. Chem.* **2010**, *75*, 8351-8354.
[27] a) M. Gsänger, D. Bialas, L. Huang, M. Stolte and F. Würthner, *Adv. Mater. (Weinheim, Ger.)* **2016**, *28*, 3615-3645; b) K.-W. Ding, T.-Q. Li, Z.-X. Ge, J.-H. Bu and Y. Liu, *RSC Adv.* **2018**, *8*, 35759-35767.
[28] a) B. L. Cannon, D. L. Kellis, L. K. Patten, P. H. Davis, J. Lee, E. Graugnard, B. Yurke and W. B. Knowlton, *J. Phys. Chem. A* **2017**, *121*, 6905-6916; b) N. V. Belko, M. P. Samtsov, G. A. Gusakov, D. S. Tarasau, A. A. Lugovski and E. S. Voropay, *J. Appl. Spec.* **2019**, *85*, 997-1005.
[29] I. I. Sahay and P. S. Ghalsasi, *ACS Omega* **2019**, *4*, 437-443.
[30] a) Z. A. Tabasi, E. A. Younes, J. C. Walsh, D. W. Thompson, G. J. Bodwell and Y. Zhao, *ACS Omega* **2018**, *3*, 16387-16397; b) S. Sahu, Ila, B. Shankar, M. Sathiyendiran and G. Krishnamoorthy, *J. Photochem. Photobiol., A* **2018**, *353*, 416-423.
[31] L. Frish, S. E. Matthews, V. Böhmer and Y. Cohen, *J. Chem. Soc. Perkin Trans. 2* **1999**, 669-672.
[32] a) L. Avram and Y. Cohen, *Chem. Soc. Rev.* **2015**, *44*, 586-602; b) Y. Cohen, L. Avram and L. Frish, *Angew. Chem. Int. Ed.* **2005**, *44*, 520-554.
[33] Y. Cohen, L. Avram, T. Evan-Salem, S. Slovak, N. Shemesh and L. Frish in *Diffusion NMR in supramolecular chemistry and complexed systems*, *Vol. 1* (Ed. C. A. Schalley), Wiley-VCH Verlag GmbH & Co. KGaA, Weinheim, **2012**, pp. 197-285.
[34] M. J. Hynes, *J. Chem. Soc. Dalton Trans.* **1993**, 311-312.